Supplementary Information for

Microring resonator as a Rayleigh mirror for broadband laser-cavity comb generation

Aram A. Mkrtchyan[1], Anastasia S. Netrusova[1], Mikhail S. Mishevsky[1], Zohran Ali[1], Nikita Yu. Dmitriev[2], Kirill N. Minkov[2], Dmitry A. Chermoshentsev[2,3], Albert G. Nasibulin[1], Igor A. Bilenko[2] and Yuriy G. Gladush[1*]

[1] Skolkovo Institute of Science and Technology, 30 Bolshoy Boulevard, building 1, Moscow, 121205, Russia.

[2] Russian Quantum Center, 30 Bolshoy Boulevard, building 1, Moscow, 121205, Russia

[3] Moscow Institute of Physics and Technology, (National Research University), Dolgoprudny 141700, Russia

These authors contributed equally: Aram A. Mkrtchyan, Anastasia S. Netrusova

*y.gladush@skol.tech

1. Forward- and backward-propagating combs with CW pump.

We pumped the chip via an edge-coupled external narrow-linewidth tunable CW laser through a circulator and scanned across the MRR resonance, observing evolution of blue-detuned regimes from the primary to modulation instability (MI) comb (see transmitted comb in Fig. S1). The backward-propagating comb had a shape of spectrum similar to the forward-propagating one and contained 1.8% of the incident power returning back to the fiber, corresponding to 8% power in the back-propagating comb in the chip (Fig. S1).

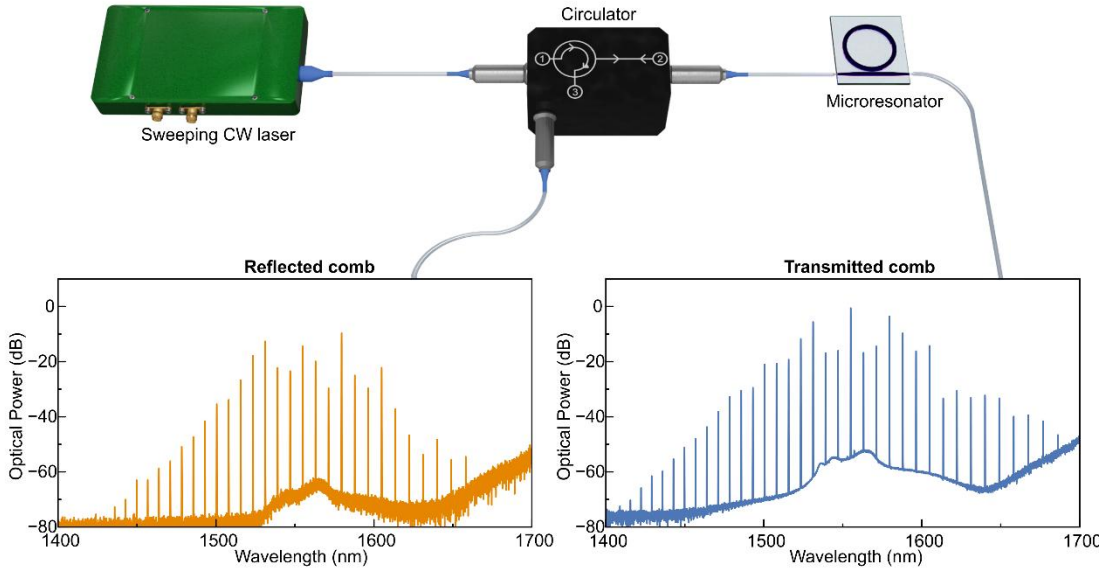


Figure S1. Reflected and transmitted spectra of external CW laser-generated frequency combs in microcavity. The setup includes the Si_3N_4 microresonator with the following parameters: 1 THz free spectral range (FSR), 1 million Q-factor, -13.5 fs^2mm^{-1} second-order dispersion (anomalous), and 0.55 bus waveguide-to-MRR coupling coefficient at 1550 nm. Tunable laser emission goes through polarization maintaining (PM) circulator followed by PM-lensed fibers butt-coupled to the chip to excite TE-mode of the microcavity.

2. Variations of hybrid-laser scheme.

We have compared our approach for the linear laser scheme (Fig. S2a) and in the

ring cavity scheme where the MRR is coupled to the laser cavity through the circulator (Fig. S2c). Both schemes demonstrated comparable soliton self-starting performance. However, the linear scheme yielded more efficient comb generation (Fig. S2b) in comparison to the ring (Fig. S2d) cavity due to additional spectral-dependent losses in the ring cavity caused by the double pass through the circulator.

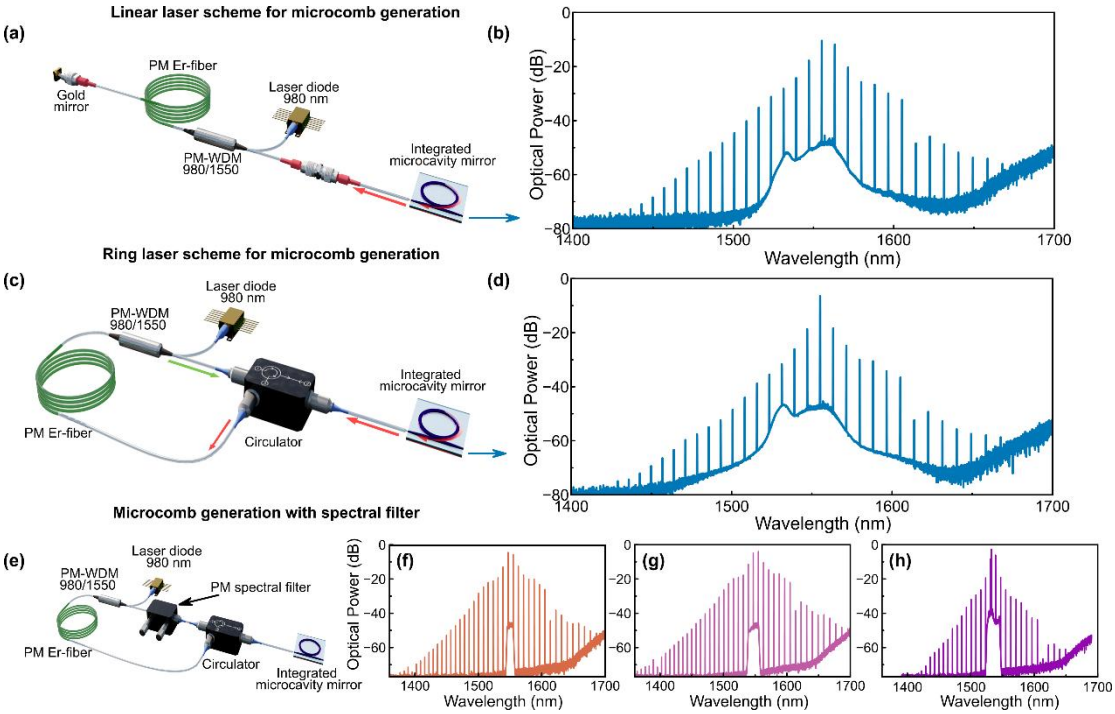


Figure S2. Variations of hybrid-laser scheme and corresponding comb spectra. **a,** Linear fiber cavity configuration and, **b,** corresponding comb spectra at 400 mA pump current; **c,** ring fiber cavity configuration with the nested microresonator providing similar soliton self-starting performance, and **d,** corresponding comb spectrum at 650 mA pump current. The less efficient comb generation in the ring scheme originates from additional losses on circulator and single pass through the gain media in ring scheme. **e**, Ring fiber-cavity configuration with the nested microresonator mirror and an intracavity tunable band-pass filter placed before the chip input. **f–h,** Microcomb spectra measured at the same pump current of 800 mA for different filter settings: **f,** 10 nm filter bandwidth; **g,** 18 nm filter bandwidth; and **h,** blue-shifted[1] filter position with respect to the central comb line.

Soliton generation requires the laser cavity to be an integer multiple of the microcavity length. To satisfy this demand, a free-space delay line is usually presented in the fiber resonator. We found that for our 25 μm radius MRR, we can always find a stable comb generation regime by a slight change (within 3 μm) in the gap width between the lensed fiber probe and the chip edge. This variation was small enough not to lead to a significant decrease in the fiber-to-chip coupling efficiency. Therefore, we did not use an additional delay line in the scheme.

We tracked how comb generation changes with the presence of a tunable spectral filter inside the fiber ring resonator (Fig. S2e-g), as previously reported in the works.[1–4] The role of the filter is to ensure power flow from the main two modes to the wings to ensure coherent comb formation. In our case we found that if the filter transmits at least two comb lines, the comb is formed with little difference to the comb without filter (Fig. S2e-f). We suggest that 1 THz FSR is large enough so that sufficient spectral filtering is provided by the gain bandwidth. We also observed that the stability of comb generation varies with the band-pass filter position and the gain bandwidth. Specifically, stable comb generation occurs when the band-pass transmission is red-shifted relative to the gain central wavelength (Fig. S2e-f), while instability arises in the blue-shifted region (Fig. S2g), consistent with previous findings[1].

3. Numerical model of soliton generation and output pulse measurements.

Numerical model. We build numerical model using the mean-field formalism introduced for laser-cavity soliton microcombs by Bao H. and co-workers.[4] Their model couples a Kerr microresonator and an external fiber loop with gain medium via discrete supermodes. In our work, we extend that formalism by including Rayleigh back-scattering in the microresonator's equations: a portion of the clockwise (CW)

field is scattered into the counter-clockwise (CCW) mode, which then couples into the fiber cavity, amplified and fed back into the microresonator to form the fiber-laser cavity.

The intracavity field in the microring is represented by the slowly varying envelope $a_{cw}(x,t)$ propagating in CW direction and by CCW propagating field $a_{ccw}(x,t)$ induced by Rayleigh back-scattering. Here $x\in[-1,1]$ is the fast time over one round-trip of the microresonator and t is the slow evolution time over many cavity round-trips. The external fiber cavity is described by a set of 2N+1 supermodes $b_q(x,t)$ labelled by an integer index q which represents the offset of each longitudinal mode with respect to the center of microresonator resonance.

In normalized units the governing equations used in the simulations are:

$$\frac{\partial a_{cw}}{\partial t} = \left[-\frac{\kappa_{tot}}{2} - \frac{i\zeta_a}{2}\frac{\partial^2}{\partial x^2} + i|a_{cw}|^2\right] a_{cw} + iRa_{ccw} + \sqrt{\kappa_{ex}}\sum_q b_q \quad (1)$$

$$\frac{\partial a_{ccw}}{\partial t} = \left[-\frac{\kappa_{tot}}{2} - \frac{i\zeta_a}{2}\frac{\partial^2}{\partial x^2} + i|a_{ccw}|^2\right] a_{ccw} + iRa_{cw} \quad (2)$$

$$\frac{\partial b_q}{\partial t} = \left[g + 2\pi i(\Delta - q) + (\sigma - \frac{i\zeta_b}{2})\frac{\partial^2}{\partial x^2}\right] b_q - \sum_q b_q + \sqrt{\kappa_{ex}}a_{ccw} \quad (3)$$

The first two equations (1-2) describe the CW and CCW fields in the microresonator with 0.997 THz FSR. The total loss rate is κ_{tot}, κ_{ex} is the external coupling rate, ζ_a is the second-order dispersion of the microring, and the cubic term corresponds to the Kerr nonlinearity. Linear coupling R between a_{cw} and a_{ccw} models Rayleigh back-scattering. Equation (3) governs the dynamics of each fiber-cavity supermode. FSR of the fiber laser is ~70 MHz. The parameter σ plays the role of an effective group-delay dispersion and spectral filtering in the external fiber cavity, band-pass filter, and other intracavity components, while Δ sets the detuning between the fiber-cavity modes and the center of microresonator resonance. Each integer q introduces a frequency shift of one fiber-cavity FSR. The field a_{ccw} in the ring drives all supermodes through the coupling term proportional to κ_{ex}. The gain

coefficient is modeled by a constant $g(t)=g_p$. The total energy stored in the fiber cavity at given slow time is $E(t) = \sum_q \int |b_q(x,t)|^2 \mathrm{d}x$.

Initial conditions consist of a weak continuous-wave background in the CW ring mode $a_{cw}(x,0)$, a localized Gaussian seed in the CCW mode $a_{ccw}(x,0)$ and low-level complex Gaussian noise in all fiber-cavity supermodes $b_q(x,0)$. Initial noise seeding allows the system to evolve into a single soliton state. All parameters used in the model are listed in the Supplementary Table.

Supplementary Table. Parameters used in numerical simulations.

Parameter	**Value (normalized units)**	**Description**
Total microring loss κ_{tot}	1.94π	Total decay rate of the ring mode
External coupling rate κ_{ex}	$1.058\kappa_{tot}$	Linear coupling between the microring and the fiber cavity
Rayleigh back-scattering R (CW←→CCW)	κ_{tot}	Linear coupling from CW to CCW
Ring dispersion ζ_a	0.0348	Second-order dispersion of microresonator
Fiber dispersion ζ_b	0.59	Second-order dispersion of the fiber cavity
Fiber-cavity dispersion/filtering σ	0.034	Effective GVD + spectral filtering acting on supermodes (b_q)
Number of fiber-cavity supermodes N	N=6 → 2N+1=13 supermodes	-
Gain in fiber cavity g_p	0.395	Constant (unsaturated) EDFA gain
Detuning Δ	0.415	Relative alignment between

		center of microresonator resonance and fiber cavity

Linearization and modulational-instability (MI) map used to select operating points. To identify parameter ranges (detuning, gain, dispersion, coupling) that support self-starting solitons, we performed a standard MI analysis by linearizing Eqs. (1)-(3) around the homogeneous ('zero-pattern') state[5]. The Kerr terms vanish to first order at this operating point, so the linear operator contains only linear loss/dispersion, Rayleigh back-scattering, coupling, and loop gain/filtering.

We analyze stability by linearizing the equations and assuming perturbations $e^{i\omega x+\lambda t}$, where spatial frequency $\omega = 2\pi f_x$:

$$\{a_{cw}, a_{ccw}, b_q\} \quad (t,x) = \{\widetilde{a_{cw}}, \widetilde{a_{ccw}}, \widetilde{b_q}\} \qquad exp(\lambda(\omega)t + i\omega x) \quad (4)$$

and assemble the state vector

$$\boldsymbol{X} = [\widetilde{a_{cw}}, \widetilde{a_{ccw}}, \widetilde{b_{-N}} \dots \widetilde{b_N}] \in \mathbb{C}^{(2+M)} \quad (5)$$

Spatial derivatives act as $\partial \mapsto \omega$ and $\frac{\partial^2}{\partial x^2} \mapsto -\omega^2$. With this convention the eigenproblem reads as

$$\lambda(\omega)\boldsymbol{X} = L(\omega)\boldsymbol{X},\ L(\omega) \in \mathbb{C}^{(2+M)x(2+M)},\ M = 2N+1 \quad (6)$$

and we obtain block matrix: $$L(\omega) = \begin{bmatrix} L_{cw} & iR & \sqrt{\kappa_{ex}} \\ iR & L_{ccw} & 0 \\ 0 & \sqrt{\kappa_{ex}} & diag(L_{b_q}) - \sum_q b_q \end{bmatrix} \quad (7)$$

where the diagonal blocks are

$$L_{cw} = -\frac{\kappa_{tot}}{2} - \frac{i\zeta_a}{2}\omega^2 \quad (8)$$

$$L_{ccw} = -\frac{\kappa_{tot}}{2} - \frac{i\zeta_a}{2}\omega^2 \quad (9)$$

$$L_{b_q} = g + 2\pi i(\Delta - q) + (\sigma - \frac{i\zeta_b}{2})\,\omega^2 \quad (10)$$

For each (Δ, g) and each ω we compute the spectrum of L(ω) and define the MI gain as the largest growth rate $G(\omega;\Delta,g) = \max_k \mathrm{Re}\,\lambda_k(\omega;\Delta,g)$. Modulational instability is present if G>0. The frequency of the fastest-growing perturbation is $|f_x(\Delta,g)| = \arg\max_{\omega\geq 0} G(\omega;\Delta,g)$.

The MI threshold curve used in the (Δ, g) maps is defined by the sign change of the maximal real part at zero spatial frequency:

$$\max_k \mathrm{Re}\,\lambda_k(\omega = 0;\Delta,g_{thr}) = 0, \quad g_{thr}(\Delta) = min\,\{g: G(0;\Delta,g) > 0\} \quad (11\text{-}12)$$

Scanning the (Δ, g) plane produces the MI lobes used to choose operating points for the time-domain simulations (see Fig. S3). Their curvature and contrast are set by the ring and loop dispersion $\zeta_{a,b}$ and by the filter parameter σ.

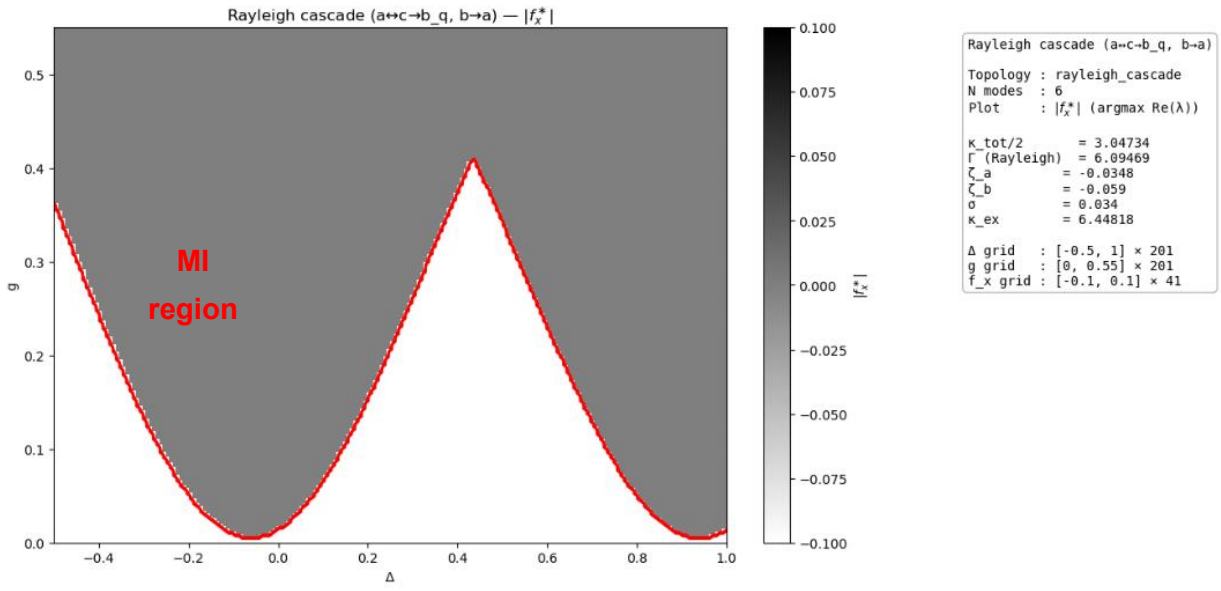


Figure S3. MI map. Grayscale shows the spatial frequency of the fastest-growing perturbation, $|f_x|$, obtained from the largest real eigenvalue of the linearized operator. The

red curve marks the modulational-instability (MI) boundary where max Re(λ) =0. The MI lobes are centered near Δ≃0 and Δ≃0.5.

4. Autocorrelation measurement of output pulse train with an external EDFA.

The pulse energy on microresonator output is insufficient for direct autocorrelation (ACF) measurements, so the pulse train is first amplified using an external EDFA. Because the EDFA bandwidth is significantly narrower than the full microcomb spectrum, only a portion of the comb is amplified (Fig. S4a, blue line). In resulting comb three main lines are 15 dB higher than other comb line, this spectral truncation leads to an artificially broadened pulse train (Fig. S4b, blue line).

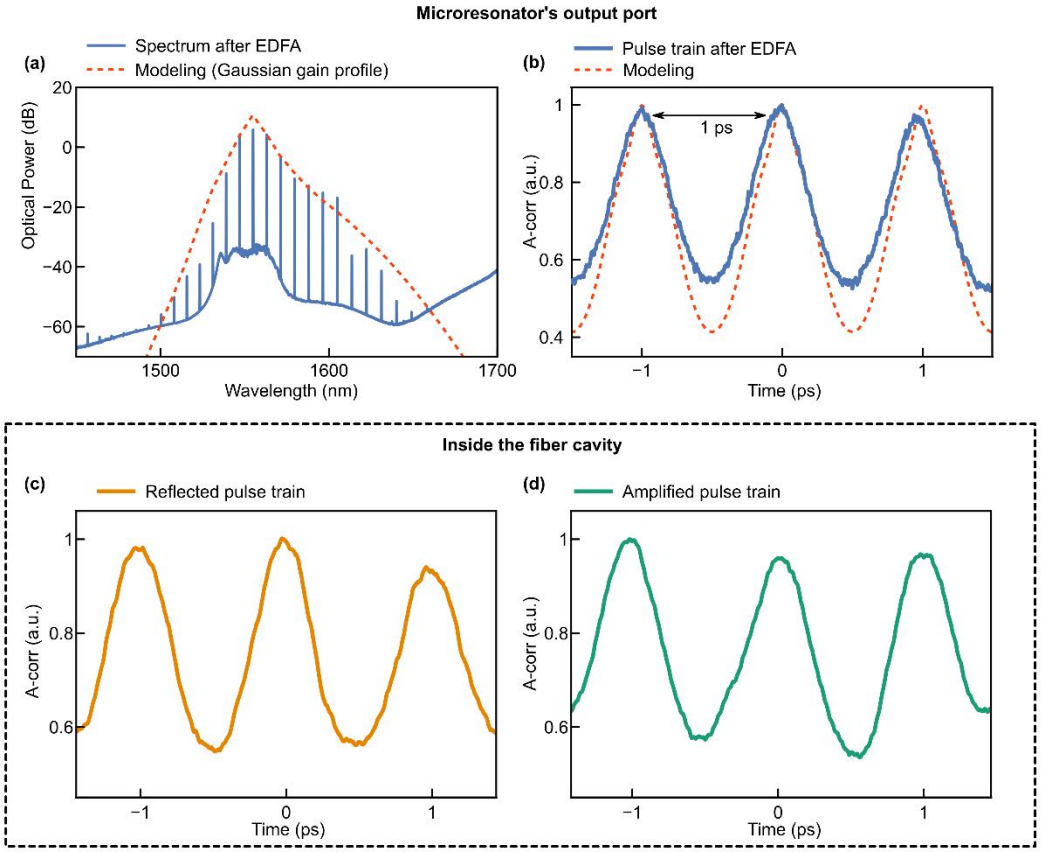


Figure S4. Autocorrelation measurements at the microresonator's output and inside

the fiber cavity. a, Spectrum at the microresonator output after external EDFA amplification (blue) together with the simulated spectrum obtained by passing the modeled output field through a numerical EDFA (red dashed). The EDFA bandwidth amplifies only a portion of the full microcomb, resulting in a spectrally truncated pulse. **b,** Autocorrelation of the EDFA-amplified pulse train measured experimentally (blue) and the corresponding autocorrelation computed from the EDFA-filtered simulated pulse (red). The agreement shows that the measured ACF to the spectrally truncated pulse rather than to the intracavity soliton. **c,** normalized ACF of the reflected comb inside the cavity, showing a clear 1 ps periodicity. **d,** Normalized ACF of the pulse train after the active fiber section in the fiber cavity, which also exhibits the same 1 ps repetition rate.

To quantify the effect of the EDFA, we take the simulated microresonator output field and apply a numerical EDFA model with a Gaussian gain profile reproducing the gain spectra width and shape of the amplifier (Fig. S4a, inset). The resulting spectrum matches the experimentally observed spectrum after amplification (Fig. S4a, red dashed line), and the autocorrelation of this EDFA-filtered simulated pulse coincides with the measured ACF (Fig. S4, red line).

In addition to measuring the EDFA-amplified output, we also record the autocorrelation of the reflected comb and of the pulse train after the active fiber section inside the laser (Fig. S4c-d). Although these intracavity traces do not provide the true pulse shape due to their limited spectral bandwidth, they exhibit a clear 1-ps periodicity. This demonstrates that the system supports a pulsed regime not only at the microresonator output but also on the pulses circulating within the fiber cavity and re-entering the microresonator.

5. Time-domain reconstruction from measured comb spectra.

To assess the consistency between our spectral measurements and the time-domain model, we reconstructed the intracavity pulses by taking the inverse

Fourier transform of the measured comb spectra under the assumption of a flat spectral phase, φ(μ)=0 for all comb lines, corresponding to the case of a fully coherent comb. For transmitted, reflected, and amplified comb, we resample it on a uniform frequency grid, and then build a spectrum $E(\nu) \propto \sqrt{P(\nu)}$ with zero phase. The temporal waveform E(t) is obtained by the inverse discrete Fourier transform, and the intensity trace $|E(t)|^2$ is normalized to unity peak power. The resulting pulse trains (solid lines in Fig. S5) are plotted together with the corresponding time-domain pulses taken directly from the numerical model (dashed lines).

This comparison shows that, even without including a non-trivial phase, the pulse shapes reconstructed from the spectra closely reproduce the simulated model pulses. In particular, for the transmitted and amplified combs the full-width at half-maximum (FWHM) durations obtained from experimental and simulated spectra are in good agreement (Fig. S5a,c), and the pedestal structure is also reproduced. For the reflected comb (Fig. S5b), the reconstructed pulse is somewhat broader than in the model, which is reasonable given that the cavity model does not take into account all experimental effects; nevertheless, the characteristic pedestal is still present. Also, the phase in our experiment was not retrieved and remains unknown, these pulse shapes can be considered as a limiting case for our system under full coherence assumption.

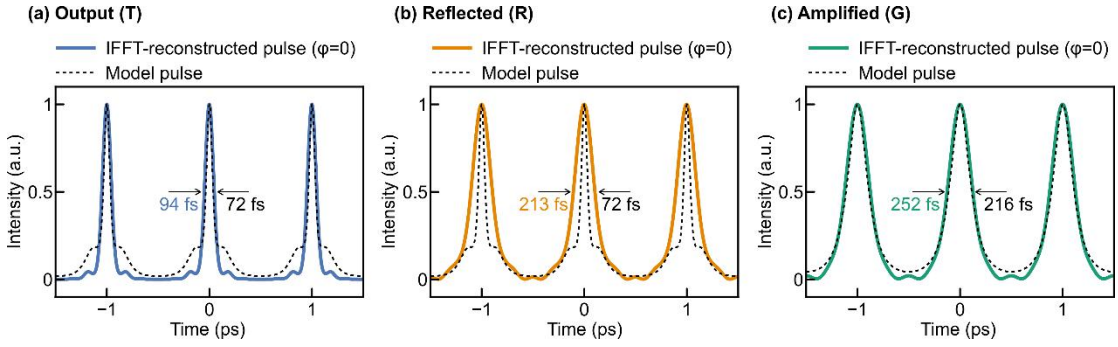


Figure S5. Temporal pulse reconstruction from comb spectra assuming flat spectral phase, φ(μ)=0. Solid lines: pulses obtained from the experimental spectra of, **a,** the output, **b,** reflected, and, **c,** amplified combs. Dashed lines: corresponding time-domain pulses taken

directly from the numerical model.

6. Laser-scanning spectroscopy measurements.

We confirm soliton comb generation by using laser scanning spectroscopy[4,6] to measure the offset (Δ) of the comb lines relative to the MRR resonance center and we analyzed the beating signal between the external CW laser and the microcomb lines (Fig. S6a). Generally, blue-detuned states correspond to a positive frequency offset (Δ>0), while red-detuned states correspond to a negative offset (Δ<0) indicating that the system operates in the soliton regime, where the Kerr nonlinearity balances the cavity dispersion, enabling stable soliton formation.[7,8]

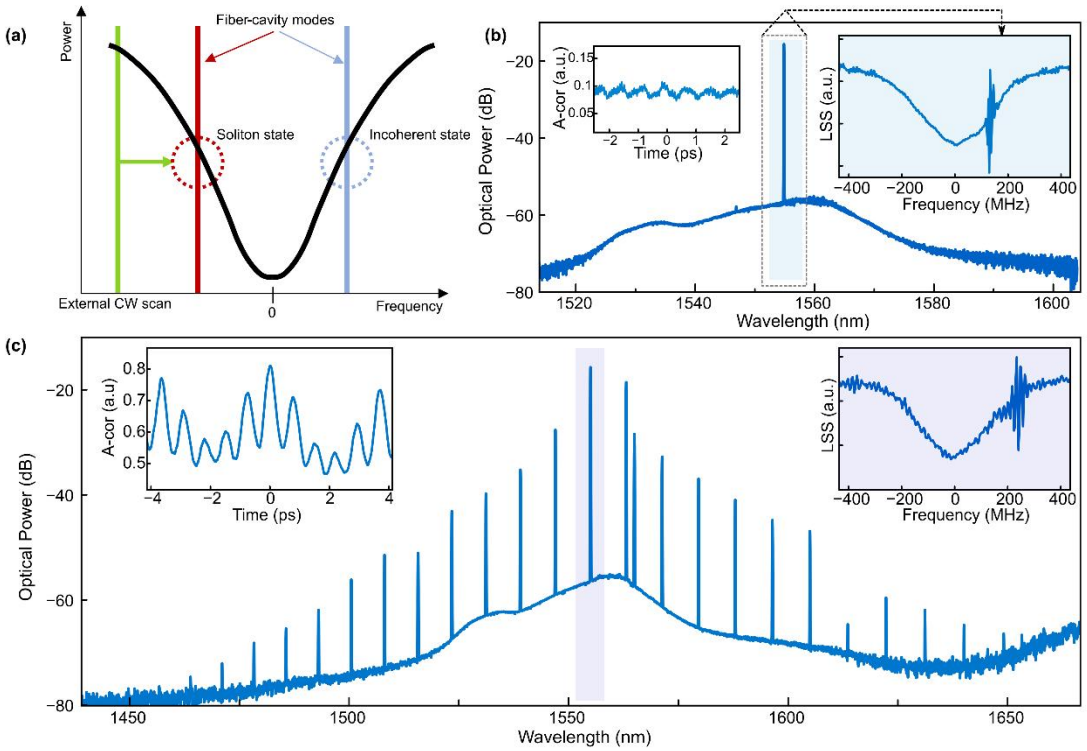


Figure S6. Laser-scanning spectroscopy technique. **a,** Schematic representation of the spectral distribution of a cold MRR resonance (black curve) with fiber-cavity modes depicting different offsets relative to the microcavity resonance center. The red curve represents the red-detuned soliton state, the blue curve represents the blue-detuned incoherent state, and the green line indicates the external tunable CW laser. Beating signals arise at the

dotted points where the CW laser scan intersects the fiber-cavity mode within the MRR resonance. **b,** Output comb spectra and their corresponding autocorrelation traces (top-left inset) and laser-scanning spectroscopy (LSS) traces (top-right inset). **c,** Spectral measurements for both soliton and incoherent states. Insets illustrate autocorrelation traces (left) and LSS results (right). The LSS traces validate transitions between coherent soliton states and incoherent states.

To perform these measurements, an external tunable CW laser with a 10 kHz linewidth was introduced into the fiber cavity via a fiber optic circulator connected to a 70/30 coupler (Fig. S7). We used elements with low wavelength dependence: insertion loss increased from 0.4 dB at 1550 nm to 1.4 dB at 1300 nm for the coupler and from 2 dB to 4 dB for the circulator. The power of the CW laser entering the MRR did not exceed 1.5 mW, ensuring that it did not affect the shape of the hot resonance. The CW laser frequency was swept across one of the MRR resonances during comb generation, demonstrating a beating when coincided with a comb line. Simultaneously, the output characteristics were measured using a spectrometer, a power meter, an oscilloscope, and an autocorrelator.

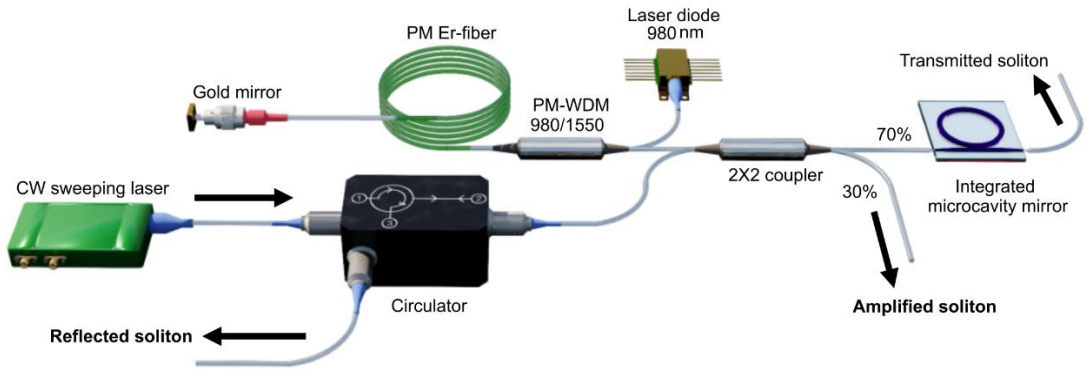


Figure S7. Setup for investigating intracavity comb power, spectral dynamics, and laser-scanning spectroscopy. The experimental setup comprises a nonlinear MRR functioning as a semitransparent mirror, an erbium-doped fiber amplifier (EDFA), and a gold mirror providing optical feedback. A 2×2 optical coupler was integrated to simultaneously

measure intracavity characteristics and perform laser scanning spectroscopy by sweeping the CW laser across the MRR resonances. This configuration enables the detection of the operating laser mode's position relative to the MRR resonance.

In addition to the soliton combs with red-detuning discussed in the main text, by tuning the position of the lensed fiber probe we also observed comb and CW states with blue-detuning illustrated in Fig. S6b-c, which exhibit distinct spectral and temporal characteristics compared to the soliton regime. Cavity length and losses play a critical role in determining the system's operating regime and enabling transitions between soliton states and noncoherent states.

7. Reflection and Transmission characteristics.

In Fig. S8a we demonstrate reflected and transmitted power fractions as measured in the fiber as a function of incident power from fiber to chip. The orange line corresponds to the total useful power (R+T) and stays around 12% regardless of the pump. The remaining losses (88%) come from the losses in the chip and coupling. To prove that nonlinear behavior of reflected and transmitted power from MRR on the pump is an intrinsic property of MRR-laser hybrid system and cannot be referred, for example, to variations of the coupling to the chip induced by the heating, we measured reflection and transmission as a function of incident power using external sources (ASE source and CW laser) that did not form a feedback system with the microresonator (Fig. S8b-c). As expected, in these cases, the reflection and transmission remained constant and did not exhibit power-dependent changes. The reflection of approximately 1%, we attribute to the reflection from the chip facet.

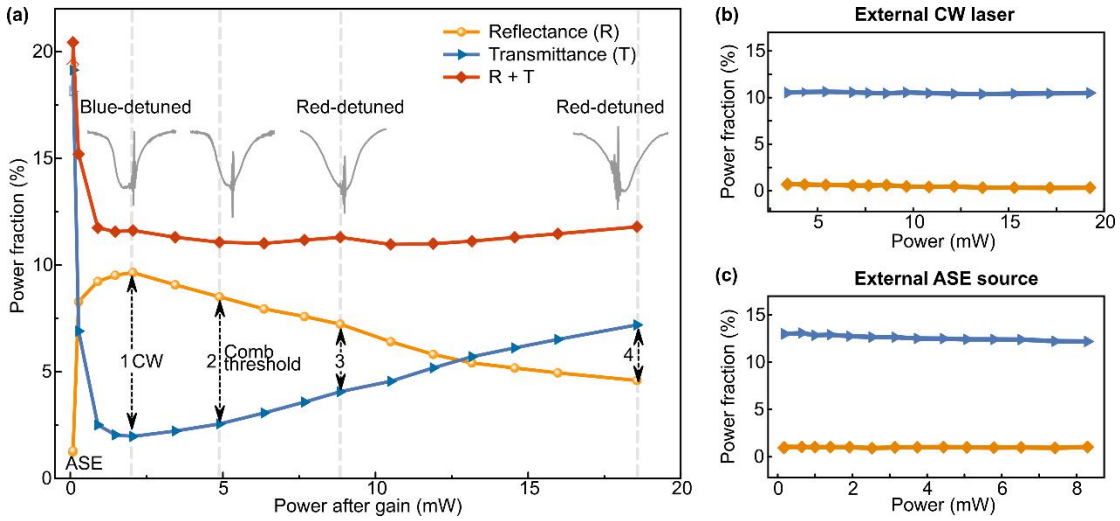


Figure S8. Measured reflection and transmission power fractions in comb generation regime and under external light sources. a, Reflection (red line), transmission (blue line), and their sum (orange line) are shown as a function of the fiber intracavity power after amplifier. The inset shows the evolution of the mode detuning for different regimes: blue-detuned CW state and red-detuned comb state. Power fractions of reflected (red) and transmitted (blue) light measured in the fiber using an external, **b,** CW laser and, **c,** ASE source**.**

References

1. Peccianti, M. et al. Demonstration of a stable ultrafast laser based on a nonlinear microcavity. *Nature Communications* **3**, 765 (2012).

2. Rowley, M. et al. Self-emergence of robust solitons in a microcavity. *Nature* **608**, 303–309 (2022).

3. Bao, H. L. et al. Laser cavity-soliton microcombs. *Nature Photonics* **13**, 384-389 (2019).

4. Cutrona, A. et al. Nonlocal bonding of a soliton and a blue-detuned state in a microcomb laser. *Communications Physics* **6**, 259 (2023).

5. Cutrona, A. et al. Temporal cavity solitons in a laser-based microcomb: a path to

a self-starting pulsed laser without saturable absorption. *Optics Express* **29**, 6629–6646 (2021).

6. Bao, H. L. et al. Turing patterns in a fiber laser with a nested microresonator: robust and controllable microcomb generation. *Physical Review Research* **2**, 023395 (2020).

7. Yi, X. et al. Soliton frequency comb at microwave rates in a high-*Q* silica microresonator. *Optica* **2**, 1078-1085 (2015).

8. Herr, T. et al. Temporal solitons in optical microresonators. *Nature Photonics* **8**, 145-152 (2014).